Fabrication of low thermal expansion Fe–Ni alloys by in-situ alloying using twin-wire arc additive manufacturing

Sood, Arjun; Schimmel, Jim; Bosman, Marko; Goulas, Constantinos; Popovich, Vera; Hermans, Marcel J.M.

DOI
10.1016/j.matdes.2024.112837

Publication date
2024

Document Version
Final published version

Published in
Materials and Design

Materials & Design 240 (2024) 112837

Contents lists available at ScienceDirect

Materials & Design

journal homepage: www.elsevier.com/locate/matdes

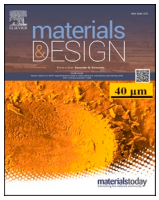

Fabrication of low thermal expansion Fe–Ni alloys by in-situ alloying using twin-wire arc additive manufacturing

Arjun Sood [a,*], Jim Schimmel [a], Marko Bosman [b], Constantinos Goulas [c], Vera Popovich [a], Marcel J.M. Hermans [a]

[a] Department of Materials Science and Engineering, Delft University of Technology, The Netherlands
[b] GKN Aerospace, Fokker Aerostructures B.V., The Netherlands
[c] Faculty of Engineering Technology, University of Twente, The Netherlands

ARTICLE INFO

Keywords:
T-WAAM
Fe-Ni alloys
In-situ alloying
Thermal expansion
Functional grading

ABSTRACT

The binary Fe–Ni system offers alloys with notably low linear coefficients of thermal expansion (CTE), contingent upon their Ni content. In this respect twin-wire arc additive manufacturing (T-WAAM) presents the opportunity of in-situ alloying through the simultaneous feeding of two metal wires into a weld pool to obtain desired alloy compositions. This study aims to deposit a graded wall with Ni contents targeted at 42, 46, and 52 wt% in the building direction of the wall, along with a block comprising of 46 wt% Ni, employing the T-WAAM approach. The results show effective incorporation of additional Ni into the weld pool and geometrically stable weld beads in the continuous metal transfer mode during the T-WAAM process. This mode led to the defect-free and chemically stable deposition of the graded wall and the block with average Ni contents of 42.3 ± 1.1, 45.8 ± 1.4, 52.6 ± 0.8 wt%, and 46.4 ± 0.9 wt%, respectively. The measured Curie temperatures of the as-deposited alloys and the mean CTE values of alloy 46 were found to be comparable to the commercial alloys. In summary, this study validates the feasibility of in-situ deposition of low thermal expansion alloy compositions, thereby enabling the possibility of on-demand thermal expansion properties.

1. Introduction

The low thermal expansion (LTE) Fe-Ni alloys are used in applications where the component geometry must remain stable under thermal loads [1,2]. In particular, the aerospace industry utilises LTE Fe-Ni alloys to fabricate molding tools for producing composite aircraft parts, ensuring adherence to stringent dimensional tolerances [3,4]. These alloys exhibit stability due to their low coefficient of thermal expansion (CTE) which is inherent to the alloys belonging to the Fe-Ni system [5]. During heating and cooling, the volume change due to spontaneous magnetostriction counteracts the dimensional change arising from lattice vibrations in the LTE Fe-Ni alloys, thereby resulting in the low CTE values [6,7]. Invar 36 contains 36 wt% Ni and displays the lowest CTE between room temperature (RT) and 150 °C of all the LTE alloys nominally composed of Fe and Ni [5]. In comparison, alloy 46, which consists of 46 wt% Ni, exhibits a lower CTE than Invar 36 in temperature ranges from RT to 300 or 400 °C [8]. A comparison between the CTE in different temperature ranges and the Curie temperature of the two alloys is given in Table 1. The Curie temperature delineates the transition from ferromagnetism to paramagnetism, or in other words, the loss of magnetic ordering in a ferromagnetic material on heating [9]. The Curie temperature of LTE Fe-Ni alloys increases with the Ni content, as shown in Table 1. For temperatures above 300 °C, alloy 46 offers better thermal expansion properties in comparison to Invar 36. Therefore, the dependence of the thermal expansion on the Ni content in the Fe-Ni system can be exploited for site specific/desired thermal expansion properties. Additionally, LTE Fe-Ni alloy products are traditionally fabricated using machining processes [10]. Due to the single-phase austenitic microstructure of these alloys, machining becomes cumbersome as the alloys tend to adhere to the tool surface, thereby degrading the tool life severely [11]. As a result, subtractive manufacturing of LTE alloys is generally associated with long lead times and high costs.

Therefore, the utilisation of additive manufacturing (AM) processes is justified for efficient processing of LTE Fe-Ni alloys. Wire and arc additive manufacturing (WAAM) is a type of directed energy deposition (DED) AM technique that involves the use of an electric arc as the heat

* Corresponding author.
E-mail address: a.sood@tudelft.nl (A. Sood).

https://doi.org/10.1016/j.matdes.2024.112837
Received 20 September 2023; Received in revised form 24 February 2024; Accepted 8 March 2024
Available online 13 March 2024

Table 1
Thermal properties of commercially available Invar 36 and alloy 46[5,8].

Thermal properties	Mean CTE, μm m^{-1} $°C^{-1}$		Curie temperature
	30 to 300 °C	30 to 400 °C	°C
Invar 36	6.1	8.7	280
Alloy 46	7.5	7.5	460

source to melt metal wires and create 3-dimensional structures [12]. The process is superior to powder based technologies in terms of the deposition rate and material costs [13]. Another advantage of utilising the WAAM process is the possibility of functionally grading a structure, which then offers site-specific material properties [14]. This can either be achieved by controlling the composition, for example by combining different alloys or by tailoring the microstructure, for example by controlling the texture [15]. In WAAM, both the possibilities of obtaining functional grading exist by either using different metal alloys or by the control of process parameters to alter the microstructure of a construct [16]. In the case of LTE Fe-Ni alloys, functional grading maybe achieved by altering the amount of Ni or by combining Invar 36 with a high-expansion alloy. For the latter, Bobbio et al. [17,18] used DED-laser powder deposition to generate functionally graded materials (FGM) by combining V and Ti-6Al-4V to Invar 36 in two different studies. Cracking was found to occur in both the cases due to the formation of detrimental intermetallic phases in the gradient region. However, the authors were successful in computationally predicting the experimentally observed phases in the gradient regions. In another study, Hofmann et al. [19] created a radial gradient from stainless steel 304L (SS304L) to Invar 36 using DED-laser powder deposition. Despite the mismatch in the CTE of the two alloys, crack-free FGM of SS304L/Invar 36 was successfully deposited. Furthermore, in-situ alloying can be used in WAAM to synthesise desired alloy compositions. This involves the simultaneous feeding of two metal wires in a single melt pool to deposit 3D structures and is commonly known as the Twin-WAAM or T-WAAM process [20]. The use of T-WAAM can facilitate the on-demand generation of LTE alloy compositions by combining elemental Fe and Ni wires or Invar 36 with a Ni wire. This, in turn, opens up possibilities for cost-effective utilisation of the thermal expansion properties of Invar-type alloys. However, the literature related to the in-situ fabrication of LTE Fe-Ni alloys is lacking, in contrast to the studies available on FGM deposition using Invar alloy. Therefore, in this study we use in-situ alloying enabled through a twin-wire approach in the cold wire pulsed current gas tungsten arc welding (GTAW) to deposit the Fe-Ni LTE alloys. A graded wall comprising 42, 46, and 52 wt% Ni in the building direction, along with a block containing 46 wt% Ni, is deposited. This is achieved by varying the wire feed speeds of two wires: 36 wt% Ni or Invar 36 wire, and approximately 96 wt% Ni wire. The microstructure of the as-deposited alloys is characterised through optical microscopy and X-ray diffraction (XRD). The stability of the process in the twin-wire approach is established through melt pool imaging and the as-deposited compositions are quantified using energy dispersive spectroscopy (EDS). Lastly, dilatometry is used to measure the Curie temperatures of the resulting compositions in the graded wall and quantifying the mean CTE of alloy 46 from the as-deposited block. In brief, we systematically addresses the weld pool stability during the T-WAAM process and chemical mixing, along with the resulting functional properties of in-situ fabricated LTE alloys. Consequently, establishing the feasibility of utilising the T-WAAM process for the on-demand generation of LTE alloys. Not only does this study offer promise for the efficient fabrication of new molding tools, but it also presents opportunities for the repair and maintenance of existing LTE alloy tools. By enhancing the usability and versatility of T-WAAM, this research contributes to the ongoing evolution of additive manufacturing technologies in aerospace applications.

2. Methods

2.1. Material fabrication

A Migatronic TIG COMMANDER AC/DC 400 was used as the power source for the deposition. All the experiments were performed in the pulsed current mode using argon as a shielding gas at a flow rate of 10 L min^{-1} and a tip angle of 30° for the tungsten alloy electrode. The consumables used in this study were metal wires of 1.2 mm diameter supplied from Voestalpine Böhler Welding. The wires are commercially known as 3Dprint AM Mold 36 (alloy Fe-Ni36), the Invar 36 wire, and UTP A 80 Ni, approx. 96 wt% Ni wire. The chemical compositions of the wires are listed in Table 2. The process parameters used in this study are listed in Table 3 and were derived from our previous work on DED-WAAM (cold wire GTAW) of Invar 36 [21]. A functionally graded two beads thick wall and a block of $100\times12\times28$ mm^3 and $120\times12\times12$ mm^3, respectively, were deposited using the T-WAAM process. The wire feed speeds were adjusted in order to achieve desired Ni amounts of 42, 46 and 52 wt% along the building direction of the wall and 46 wt% in the block. The functionally graded wall and the alloy 46 block are shown in Fig. 1(a) and (b), respectively. The inter-pass temperature was limited to 120 °C during the deposition and monitored using a K-type thermocouple [22].

2.2. Sample preparation and characterisation

The microstructural features of the graded wall and the block were studied using optical microscopy. Two cross-sections were taken at 35 and 65 mm (parallel to the BD) from the starts of the deposits for the analysis of the microstructure. The dimensional characteristics of the weld beads obtained from the bead-on-plate experiments were determined by analysing the optical images using the ImageJ software. Four cross-sections were taken at 35, 45, 55 and 65 mm (parallel to the BD) from the starts of the deposits for evaluating the weld bead dimensions. A Keyence VHX-5000 digital optical microscope was used in this study for the purpose of optical microscopy. The sample preparation comprised of mechanical grinding using SiC papers (P180 to P4000), followed by polishing using a 3 and 1 μm diamond suspension for 6 and 10 min, respectively. Chemical etching was performed with the Kalling's No. 2 reagent for approximately 5–10 s. EDS was used for the qualitative and quantitative analysis of the chemical composition of the deposits. A ThermoFisher Scientific™ Helios™ G4 Plasma FIB UXe Scanning Electron Microscope (Helios-SEM) was used for this purpose at an acceleration voltage of 20 kV and beam current of 0.80 nA. Phase analysis was performed using XRD. The cross-section taken at 45 mm from the start of the graded wall was used to obtain the diffraction patterns at locations corresponding to the regions that were intended to contain the desired Ni contents of 42, 46 and 52 wt%. A Bruker D8 Advance diffractometer was used for this purpose. The instrument utilised Cu Kα radiation and the acquisition parameters during the XRD analysis were a step size of 0.04° and counting time of 5 s per step. Lastly, electron backscatter diffraction (EBSD) with simultaneous EDS was also used for phase and microstructure analysis of the in-situ deposited alloys. Metallographic samples for EBSD were further polished with a colloidal silica suspension for 45 mins in addition to the preparation procedure mentioned above. The Helios-SEM is equipped with an AMETEK-EDAX camera and was used for the purpose of EBSD. The samples were tilted to an angle of 60° and a step size of 0.8 μm was used to scan areas of 1.4×1.3 mm^2 corresponding to alloys 42, 46 and 52 of the graded wall. The raw data was post-processed using EDAX-OIM Analysis™ software version 8.6. The beam current and acceleration voltage during the EBSD measurements with simultaneous EDS were 3.2 nA and 20 kV, respectively.

2.3. Melt pool imaging

The liquid metal transfer characteristics during the T-WAAM process

Table 2
Manufacturer specifications for the chemical composition of the consumables used in this study (*element content is less than the specified number).

Elements, wt.%	C	Si*	Mn	Cr*	Mo*	Co*	P*	S*	Ni	Fe	Ti
Alloy Fe-Ni36	0.05	0.10	0.20	0.50	0.50	1.00	0.01	0.01	34–38	Bal.	–
UTP A 80 Ni	0.02*	0.30	0.30	–	–	–	–	–	Bal.	0.10*	3.30

Table 3
Process parameters used in this study for the deposition of the graded wall and alloy 46 block. TS- travel speed, I_{Base}- base current, I_{Peak}- peak current, t_{Base}- base time, t_{Peak}- peak time, U_{Ave}- average voltage and HI- heat input.

Parameters	TS, mm s^{-1}	I_{Base}, A	I_{Peak}, A	t_{Base}, s	t_{Peak}, s	U_{Ave}, V	HI, J mm^{-1}
Wall and block	4.6	81	180	0.20	0.20	10.0	200

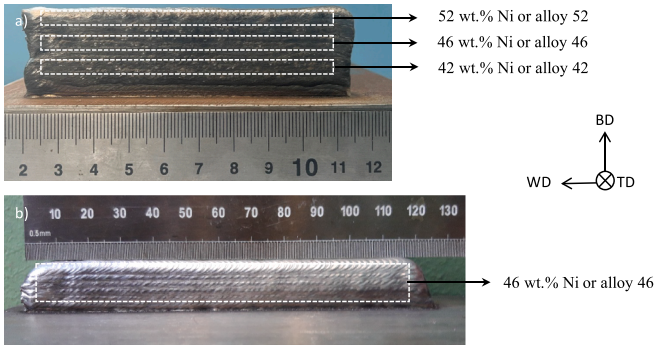

Fig. 1. (a) and (b) shows the as-deposited graded wall and alloy 46 block, respectively. BD- building direction, WD- welding/travel direction and TD- transverse direction.

were investigated using a specialised camera and illumination system. A Cavitar C300 welding camera was used for this purpose. The camera is equipped with a pulsed laser illumination system of 645 ± 10 nm wavelength. A narrow optical band pass filter is also incorporated in the camera for spectral filtering of the optical radiation from the welding arc. The gain and the exposure settings on the camera were adjusted to optimise the image quality. The maximum achievable recording rate of the camera with the laser illumination is 100 frames per second.

2.4. Dilatometry

A Bähr 805 A/D dilatometer was used for evaluating the Curie temperature of the alloy compositions in the as-deposited graded wall. The Bähr dilatometer, uses two quartz rods connected to a Linear Variable Differential Transformer (LVDT) displacement sensor and an induction coil instead of a furnace to heat up the sample. The power used in the induction coil is recorded in parallel with the temperature and the thermal expansion. Different to the principle of dilatometers that rely on furnace-based heating, this apparatus utilises two quartz rods connected to a LVDT displacement sensor and an induction coil to record the sample thermal expansion. Throughout the heating process, the temperature and thermal expansion are simultaneously recorded, along with the power consumed by the induction coil. Three cylindrical specimens of 3.5 mm diameter and 10 mm length were extracted from the graded wall using wire-electronic discharge machining (EDM). The locations of the specimens corresponded to the regions of alloys 42, 46 and 52 in the graded wall. The axis of the cylindrical specimens was oriented parallel to the welding direction (WD). The tests were performed under vacuum at a heating rate of 10 °C min^{-1}. Additionally, a Linseis TMA PT1000 thermo-mechanical analyser was used for evaluating the linear CTE of the in-situ deposited alloy 46. The TMA PT1000 uses a resistance furnace and a high resolution LVDT displacement sensor connected to a quartz piston and sample stage. Cylindrical specimens of 4 mm diameter and 10 mm length were extracted using wire-EDM from the block. The samples from the block were extracted with their axis oriented parallel to the building (BD) and the welding direction (WD) for evaluating the properties in two directions. The testing procedure was in accordance with the ASTM E831-19 standard while using argon to create an inert atmosphere in the furnace [23]. The tests were performed in a temperature range between room temperature and 550 °C with a heating rate of 5 °C min^{-1} [23]. The average linear CTE was calculated based on the displacement-temperature curves by Eq. (1):

$$\alpha = \frac{1}{L_0}\frac{dL}{dT}, \tag{1}$$

where, $\underline{\alpha}$ represents the mean CTE to desired temperature interval; L_0 is the initial length of the specimen; $\underline{dL}$ is the change in length of the specimen accompanied by the temperature variation; $\underline{dT}$ is the temperature variation.

3. Results and discussion

3.1. Bead-on-plate experiments

Bead-on-plate experiments were first performed to optimise the deposition during the T-WAAM process. The overview of the beads obtained from the bead-on-plate experiments are shown in Fig. 2. For these beads the Invar wire was fed towards the centre of weld pool, whereas the Ni wire was fed towards the edge of the weld bead. The ratio for the wire feed speeds of the two wires was adjusted to achieve the composition of alloy 42 as this would be the first composition in the graded wall to be obtained by the twin-wire approach. In Table 4, bead 3 demonstrated the highest stability, as reflected by the lowest deviation in the height, width and wetting angle of the beads. Consequently, bead 3 is considered optimum for depositing 3-dimensional structures. Melt pool imaging was performed to understand the melt pool behaviour during the bead-on-plate experiments. This technique revealed two distinct modes of molten metal transfer during the twin-wire GTAW process: intermittent metal transfer and continuous melting transfer as shown in Figs. 3 and 4, respectively. The intermittent metal transfer mode occurred during the deposition of beads 1 and 2, shown in Fig. 2. Bead 2 was more stable in comparison to bead 1 despite being deposited in the same metal transfer mode. This was due to the reduction of the distance between the Ni wire tip and the substrate during the deposition of bead 2 in comparison to bead 1, thereby reducing the droplet size during the intermittent metal transfer mode. In this mode of metal transfer, the flow of liquid metal to the weld pool is not continuous and a metal droplet is formed at the tip of the wire. The droplet remains attached to the wire due to the surface tension and detaches as it comes in contact with the weld pool. In case of bead 1, larger metal droplets form at the tip of the wire in comparison to bead 2 as shown in Fig. 3(a) and (b), respectively. The large droplets entering the melt pool in the case of bead 1 cause instabilities in the weld pool as shown in Fig. 3(a). In this figure, the detachment of a metal droplet causes oscillations of the weld pool. The instabilities in the weld pool cause abrupt spatial changes in the geometrical characteristics of the weld bead as evident in Fig. 2(a) and 3(a). Whereas, in the case of bead 2, smaller droplets are

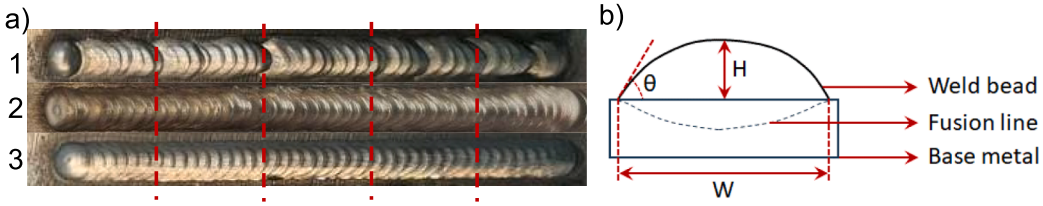

Fig. 2. Weld beads obtained from the bead-on-plate experiments using the T-WAAM process in (a), beads 1 and 2 are deposited in the intermittent metal transfer mode and bead 3 in the continuous metal transfer mode. Schematic of the measured weld bead dimensions in (b), where w- width, h- height and θ- wetting angle. The red dashed lines in (a), show the locations where the cross-sections were taken. (For interpretation of the references to colour in this figure legend, the reader is referred to the web version of this article.)

Table 4
Dimensional characteristics and the corresponding Ni content of the weld beads shown in Fig. 2(a).

Bead number	Height, mm	Width, mm	Wetting angle, °	Ni content, wt.%
1	2.0 ± 1.3	4.7 ± 1.6	44 ± 9.3	43.4 ± 3.6
2	1.7 ± 0.9	5.1 ± 1.0	40 ± 5.6	42.8 ± 2.5
3	1.5 ± 0.3	5.4 ± 0.5	38 ± 3.2	42.3 ± 1.1

formed at the tip of the wire and the weld pool instabilities are not as severe as in the case of bead 2. Consequently, the melt pool and the resulting bead geometry are more stable for bead 2 than bead 1. However, positioning of the Ni wire to achieve the intermittent transfer mode during the twin-wire approach disrupts the stability of the process due to the sudden transfer of molten metal to the weld pool. The erratic deposition of the weld beads is a direct outcome of this mode. The highest geometrical stability was observed in the case of bead 3 as evident from Table 4. The distance between the substrate and the tip of the Ni wire was further reduced than in the case of bead 2, this in turn lead to the occurrence of the continuous metal transfer mode. In this mode, liquid metal droplets do not form at the tip of the wire and the wire remains in a continuous contact with the weld pool. A liquid metal bridge persists throughout the deposition which allows for the metal transfer to the weld pool as shown in Fig. 4. This allows for a stable deposition condition with the twin-wire approach, in contrast to the instabilities that can occur during the intermittent metal transfer mode, thereby resulting in geometrically varying weld beads. In addition, the results of the EDS point scans shown in Table 4 indicate that bead 3 was closest to the intended composition of 42 wt% Ni followed by the lowest scatter among the three beads. For the beads in the intermittent transfer mode, bead 2 was better than bead 1 in terms of the proximity to the intended composition. The average time between two droplet detachment events of the Ni wire were calculated to be 541.3 ms and 934.5 ms for beads 2 and 1, respectively. The lower time in the case of bead 2 promoted better incorporation of Ni in comparison to bead 1. Whereas, the continuous transfer of Ni to the melt pool in the case of bead 3 is effective in attaining the highest compositional stability. Therefore, the continuous metal transfer mode offers the compositional and geometrical stability required for the fabrication of multi-bead structures using the twin-wire approach for in-situ alloying. These multi-bead structures

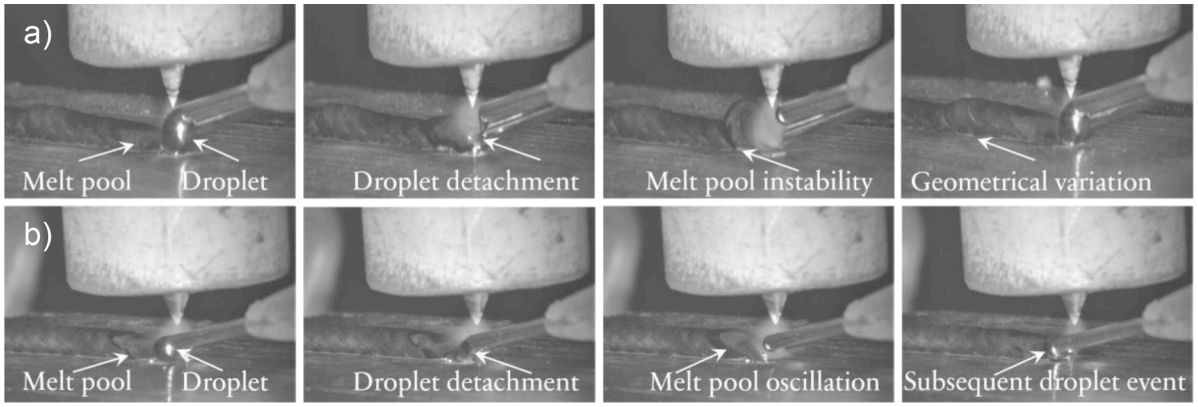

Fig. 3. Instability occurring in the melt pool due to the detachment of large droplets in (a) and comparatively mild oscillations due to the detachment of a smaller droplet in (b), during the intermittent metal transfer mode.

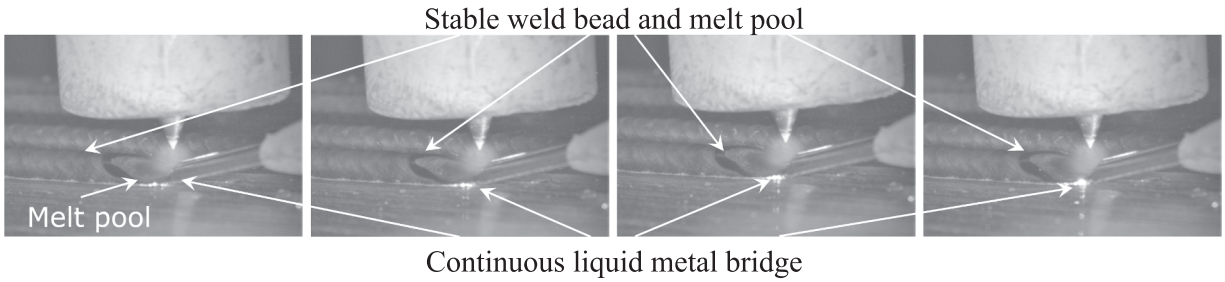

Fig. 4. Stability of the melt pool in the continuous metal transfer mode due to the formation of a persisting liquid metal bridge.

are presented and discussed in the following sections.

3.2. Macro and microstructure characterisation

The overview of the graded wall and the alloy 46 block are shown in Fig. 5(a) and (b), respectively. The deposition quality is assessed by determining the effective area fraction from four cross-sections. The total area corresponds to the cross-sectional area following the edges and contours of the deposit. Whereas, the effective area is determined by fitting a solid shape with flat sides (a rectangle in the case of Fig. 5) on the cross-section such that its edges contain the innermost points of the deposit's surface. The effective area corresponds to the usable amount of the deposit after the removal of the surface waviness due to the layer-by-layer deposition in WAAM [24]. The usable area fraction is simply the ratio between the effective and total area. Therefore, for the purpose of obtaining a solid structure after eliminating the surface waviness, a higher effective area translates to reduced material removal during post-processing [24]. The first and last layers of the deposits were excluded from the usable area fraction calculations. In terms of the usable area fractions, the graded wall performs better than the block as shown in Table 5. This could be due to the higher number of overlaps that were required to deposit the block. Nonetheless, both structures show high geometrical stability as seen from the relatively low scatters in Table 5, and this can be attributed to the low heat input used during the deposition. Achieving high usable areas is important due to the difficulties in machining and costliness of LTE Fe-Ni alloys. Using the twin-wire approach, structures with usable areas of upto 95 % were deposited in this study. The microstructure of the graded wall corresponding to the regions comprising of alloys 42, 46 and 52 are shown in Fig. 6(a), (b) and (c), respectively, and the microstructure of the alloy 46 block is shown in Fig. 6(d). The cross-sections of the wall and block did not show lack of fusion defects nor intergranular cracks. This is achieved due to the high stability of the weld beads in the continuous metal transfer mode and the low heat input used during the deposition of the structures, respectively. The microstructure of both structures mainly comprises of columnar grains that extend across multiple layers as seen in Fig. 6. Epitaxial growth of columnar grains is observed between layers and the microstructure does not change with the increasing amount of Ni as the grain morphology is similar for the three alloy compositions in the graded wall. This can be attributed to the formation of the single-phase austenitic solid solution in the binary Fe-Ni system. Typical solidification substructures comprising of cellular and columnar dendritic features are observed in the microstructures of both the deposits as pointed out in Fig. 6. The formation of these structures is a result of the relation between the thermal gradient (G) and the interface growth velocity (V)

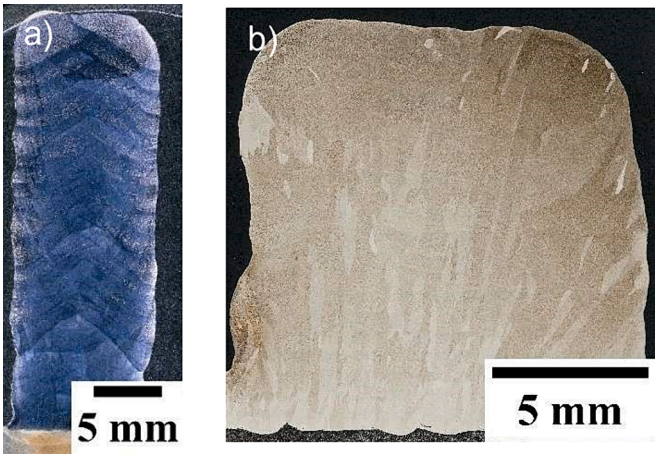

Fig. 5. Cross-sectional overview of the graded wall and the alloy 46 block in (a) and (b), respectively.

Table 5
Usable areas quantified from the transverse cross-sections of the deposits.

Deposit	Total area, mm^2	Effective area, mm^2	Usable area fraction, %
Graded wall	194 ± 3.3	185 ± 2.8	95 ± 1.7
Alloy 46 block	125 ± 4.7	111 ± 3.6	89 ± 2.5

in the melt pool, and the undercooling [25]. The G/V ratio in the melt pool controls the formation of the different grain substructures such as planar, cellular, columnar dendritic and equiaxed dendritic. As the G/V ratio decreases the morphology of the substructures transforms from planar to cellular, columnar dendritic, and finally towards equiaxed dendritic at low G/V ratios or high undercoolings [26]. Considering a single melt pool in the microstructures obtained in this study, planar solidification was observed close to the fusion lines as the thermal gradient is highest at the bottom of the melt pool. As the distance from the bottom of the melt increases the planar solidification destabilises and cellular/columnar dendritic solidification occurs due to a decrease of the G/V ratio. These microstructural features are similar to those reported in the studies on the deposition of Invar 36 alloys using powder and wire-based DED methods [27,28,29]. Additionally, the growth direction of the columnar grains (GGD in Fig. 6) deviates slightly from the building direction. This is due to the curvature of the fusion lines and the grain growth being dictated by the direction of the maximum thermal gradient in the melt pool [26]. After the initial epitaxial growth at the fusion line, the grains will have a tendency to grow in the direction of the maximum G which lies normal to the solid–liquid interface at each point. As the fusion occurs on the curved top surface of the previously deposited beads, the columnar grains grow at a deviation from the building direction. The deviation from the building direction is more pronounced in the graded wall in comparison to the block with angles of 19° and 11°, respectively. This occurs due to the single overlap of the two beads used in depositing the graded wall. Samples were extracted from the graded wall at the locations corresponding to the compositions of alloys 42, 46 and 52 for phase analysis through XRD. The detected peaks correspond to a completely austenitic structure for the three alloy compositions as shown in Fig. 7(a). This can be attributed to the stability of austenite (γ-FeNi) in the equilibrium phase diagram of the Fe-Ni system for the alloy compositions deposited in this study. The combination of Ni and Invar36 wires for in-situ deposition of low expansion alloys further helps in ensuring that the alloys exist in the single phase structure. This is due to the fcc crystal structure of both the wires. In comparison, using elemental Fe (bcc) and Ni (fcc) wires could lead to the formation of the α (bcc) phase due to incomplete mixing or segregation, as it is stable in the binary Fe-Ni alloys containing approximately less than 31 wt% Ni. Ensuring the formation of only austenite is critical for retaining the thermal expansion properties of the LTE alloys. Furthermore, Fig. 7(b) shows the results of the EBSD scans with simultaneous EDS measurements performed on alloys 42, 46 and 52 of the graded wall. The image quality maps clearly reveal the presence of long columnar grains in the LTE alloys. The phase maps also complement the XRD results as only γ phase is detected in the three alloys. This is in contradiction with the results of Qiu et al. [30] as reported in their study on selective laser melting of Invar 36. They found the absence of α phase when analysing Invar samples using XRD; however, the α phase was detected using EBSD. The Ni maps of the alloys give evidence of a qualitative increase in the amount of Ni from alloys 42 to 46 and 52. This difference is attributed to the higher amount of Ni incorporated in alloy 52 compared to alloys 46 and 42. Lastly, the Ni maps indicate a homogeneous distribution of Ni in the three in-situ deposited alloys as locally enriched regions in Ni are absent. The chemical analysis of the in-situ deposited LTE alloys by T-WAAM is further explored in the following section.

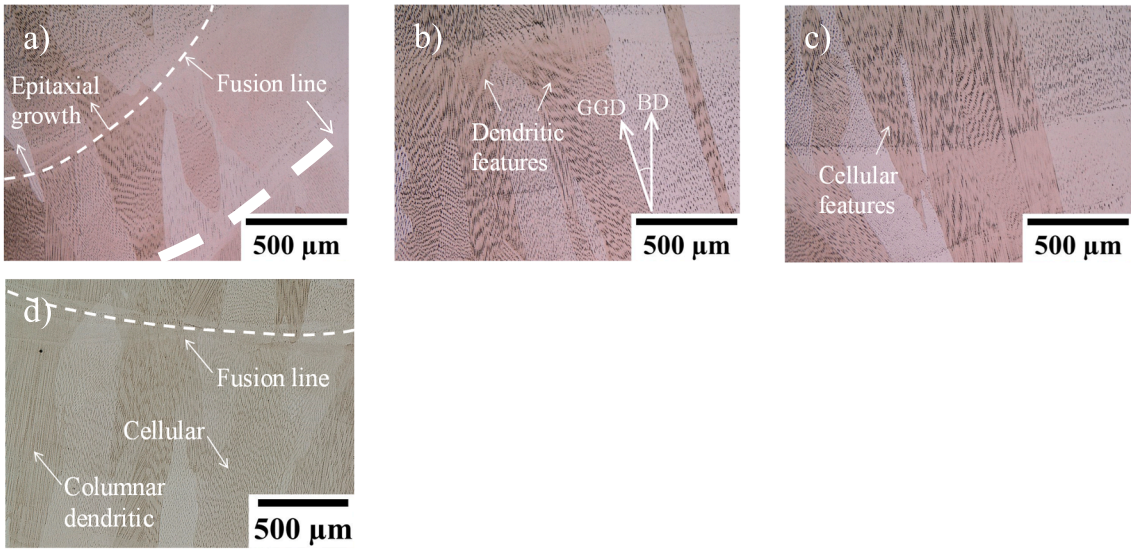

Fig. 6. Microstructure of LTE alloys 42, 46 and 52 from the graded wall in (a), (b) and (c), respectively, and the alloy 46 block in (d).

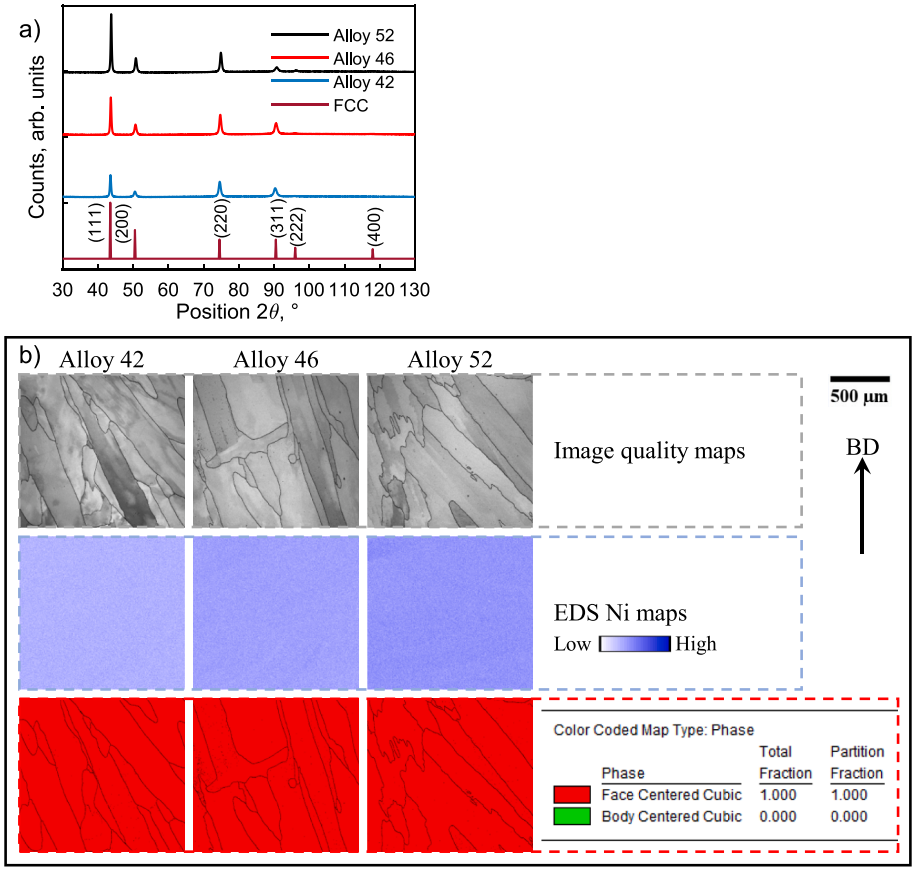

Fig. 7. XRD patterns of the as-deposited LTE alloys 42, 46 and 52 from the graded wall in (a), and the results of EBSD scans with simultaneous EDS showing the image quality maps, Ni maps and phase maps in (b).

3.3. Chemical analysis

The graded wall was intended to consist of 42, 46 and 52 wt% Ni. Five layers were deposited for each composition. The results of the EDS map scans taken at different positions on the cross-section of the graded wall are shown in Fig. 8(b). The locations where the map scans were taken for the three LTE alloys are marked by numbers as shown in Fig. 8 (a). The maps gives evidence of adequate mixing between the Invar 36 and Ni wires during the T-WAAM process as no clusters or segregated regions of Ni are observed. This behaviour is found to be consistent among the three LTE alloy compositions as seen from the map scans. The maps also provide a qualitative indication of the Ni and Fe contents in alloys 42, 46 and 52. This is reflected by the increasing Ni signals (green bar in the Ni maps) when moving from the region of alloy 42 towards 46

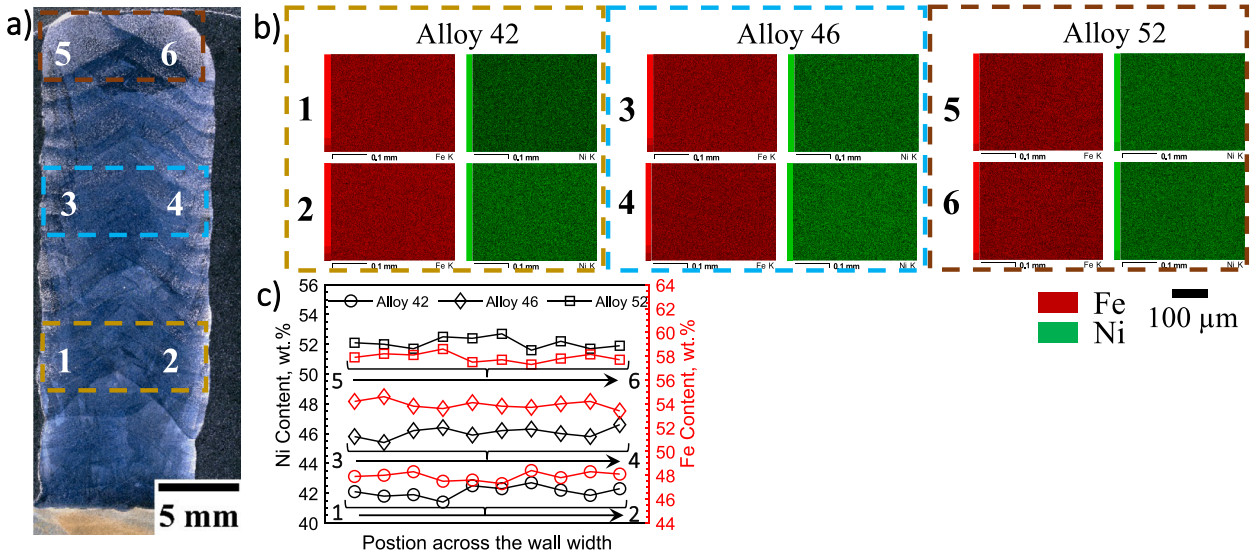

Fig. 8. (a) shows the cross-section of the graded wall with numbered locations for the EDS analysis. (b) shows the EDS maps for Fe and Ni at the locations indicated in (a), revealing mixing of the added Ni in the different LTE alloys. (c) shows the results of the point scans conducted between points 1 to 2, 3 to 4 and 5 to 6 in (a), illustrating the homogenous distribution of Ni within a single layer across the width of the wall.

and 52. Additionally, the Ni wire is fed towards the side of the weld bead, however this does not cause any difference in the distribution of Ni across the width of the wall within a single layer. This is reflected through the map scans as they show similar results when comparing locations 1 to 2, 3 to 4 and 5 to 6. Also, the quantified Fe and Ni contents in alloys 42, 46 and 52, marked in Fig. 8(a), show good stability of the elements across the width of the wall within a single layer as shown in Fig. 8(c). Therefore, the flow in the weld pool is sufficient for homogeneously distributing the added Ni during the T-WAAM process. Point scans were performed for quantifying the amount of Ni incorporated in the graded wall and the results are presented as a colour map shown in Fig. 9. Three distinct regions comprising of average Ni contents of 42.3 $\pm$ 1.1, 45.8 $\pm$ 1.4 and 52.6 $\pm$ 0.8 wt% were identified and are labelled as alloy 42, 46 and 52 in the figure, respectively. The scatter in the measurements is low and indicates that a good control over the composition can be achieved during the T-WAAM process. The first four layers were deposited by only using the Invar 36 wire. Due to dilution with the base plate the amount of Ni in the first two layers is around 30 wt%. However, in the third layer it stabilises to around 36 wt%, which corresponds to the Ni content of the Invar 36 wire. Following this, the second wire is incorporated in the process to achieve the desired LTE compositions of alloys 42, 46 and 52 by varying the wire feed speeds of the two wires. In the transition regions, the Ni content is not stable as the wire feed speeds of the Invar 36 and Ni wires are continuously adjusted to achieve the desired LTE alloys. Therefore, in these regions the Ni content gradually increases along the building direction (BD) until it approaches the required LTE alloy composition. Furthermore, the gradual change in the Ni content within the transition region implies that a sharp boundary between the thermal expansion properties can be avoided, thereby promoting compatibility among the different LTE alloy compositions. With 5 layers deposited for each composition, the transition regions comprised of approximately 2 layers, whereas the remaining three layers correspond to the regions of stable LTE alloy compositions. Thereby, achieving the desired compositions of alloys 42, 46 and 52 in the graded wall. The alloy 46 block also showed good mixing and stability of Ni incorporation as it was quantified to have an average Ni content of 46.4 $\pm$ 0.9 wt%. From a material point of view, the compositional stability of the in-situ synthesised LTE alloys is witnessed due to the solid solution compatibility between Fe and Ni as governed by the Hume-Rothery rules of forming a substitutional solid-solution [31]. Combining the inherent solid solution compatibility of Fe and Ni with the continuous metal transfer mode of the twin-wire GTAW process

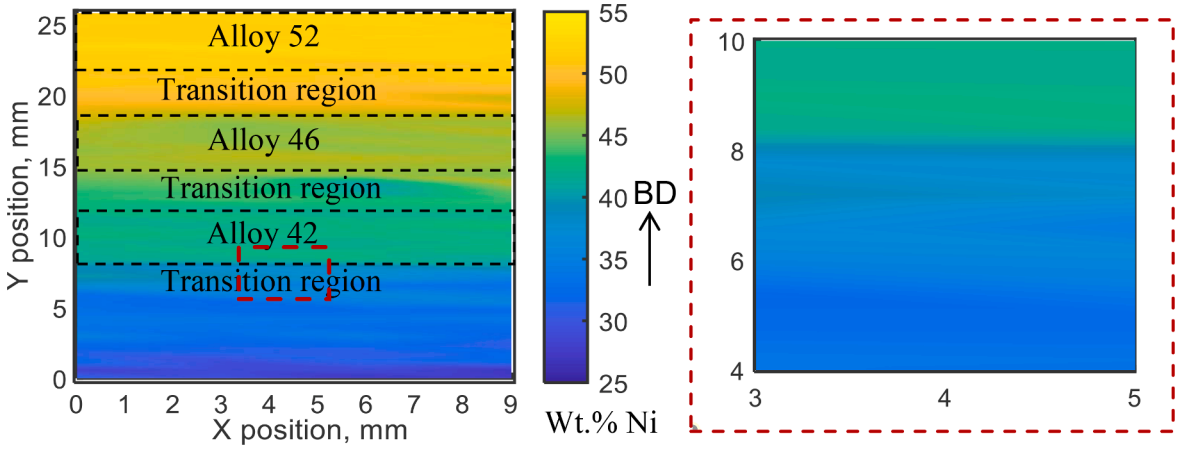

Fig. 9. Colour map showing the distribution of Ni along the building direction of the graded wall as quantified by EDS point scans. A step size of 0.5 mm was used for the point scans.

ensures good process stability and the deposition of chemically stable LTE alloys. Consequently, providing a precise control over the in-situ synthesised alloys, thereby opening the possibilities for tailoring the thermal expansion properties. In summary, using the twin-wire approach with cold wire pulsed GTAW, the desired compositions of low expansion alloys were successfully obtained.

3.4. Thermal analysis

Dilatometry was utilised to establish the Curie temperature variation within the graded wall and the mean linear thermal expansion coefficient of the block. By using an induction heated dilatometer, it is possible to locate the Curie transition of a ferromagnetic material by analysing the power supplied by the instrument. Below the Curie temperature, an induction coil heats a ferromagnetic material through the mechanisms of Joule and hysteresis heating [32]. However, only Joule heating contributes on surpassing the Curie temperature. Therefore, the instrument delivers additional power for maintaining the heating rate that is applied during the test. This manifests as a sudden jump in the supplied power at the Curie transition.

The power versus temperature plots for the specimens taken from the graded wall are shown in Fig. 10. The plots in Fig. 10(a), (b), (c) and (d) correspond to the specimens of alloys 42, 46, 52 and the transition region between alloy 42 and 46, respectively. A clear jump in the applied power is observed during the tests of alloys 42, 46 and 52 specimens. The smoothed curve before and after the power jump is fitted and tangents are drawn to the fitted curve to extract the onset and the end temperatures. The average of these two temperatures is taken as the Curie temperature and is marked on the Fig. 10(a), (b) and (c). There is no evident jump in the power for the specimen taken from the transition region as observed in Fig. 10(d). This can directly be attributed to the variation of the Ni content in this sample, thereby not showing a clear Curie transition. The values of the Curie temperatures obtained from the as-deposited LTE alloys are comparable to those of the commercial alloys as shown in Table 6. This further supports the results of the EDS analysis showing the compositional stability of the in-situ synthesised LTE compositions during the T-WAAM process. The mismatch in the measured Curie temperatures of the as-deposited alloys in comparison to the commercial alloys is likely due to the differences in the chemical compositions. The addition of elements such as Mn, Si and Ti in the LTE Fe-Ni alloys of nominal composition causes a reduction in the Curie temperature [34]. On the other hand, the presence of cobalt is known to raise the Curie temperature and simultaneously lower the thermal expansion [35,36]. In this study, the Invar 36 wire contains a maximum of 1 wt% Co, while the Ni wire contained a maximum of 3.3 wt% Ti. As a consequence, slight differences between the Curie points of the in-situ deposited alloys and the commercial alloys are reasonable due to their respective chemical compositions. Overall, the twin-wire approach in cold wire GTAW offers promising results for the in-situ synthesis of LTE alloys. The temperature-displacement curves for alloy 46 specimens oriented in the BD and WD are shown in Fig. 11. In the temperature range between RT and approximately 410 °C the alloy exhibits a low thermal expansion behaviour that is analogous to Invar 36. At temperatures higher than 410 °C, the low thermal expansion characteristic of LTE Fe-Ni alloys diminishes and a thermal expansion behaviour driven by lattice vibrations similar to that of a normal metal becomes evident. Whereas, for lower temperatures the magneto-volume effects in the alloy compensate for the thermal expansion due to lattice vibrations on heating, thereby resulting in the abnormal low thermal expansion behaviour. The mean CTE values of alloy 46 in two specimen orientations (BD and WD) are calculated from the curves shown in Fig. 11 and listed in Table 7. The alloy shows an approximately constant thermal expansion in both orientations of the specimens for temperatures between RT-300 °C and RT-400 °C, as reflected by the mean CTEs in Table 7. This is due to the characteristic Invar-type low thermal expansion behaviour of the Fe-Ni alloys. The averages of the mean CTE values between different temperature ranges are found to be higher for specimens oriented in the BD as seen in Table 7. This is consistent with

Table 6
Comparison among the Curie temperatures of the as-deposited (T-WAAM) LTE alloys and commercially available alloys.

Thermal analysis °C	As-deposited DED-WAAM			Commercial alloys [33]		
	Alloy 42	Alloy 46	Alloy 52	Alloy 42	Alloy 46	Alloy 52
Curie temperature	371 ± 3.1	441 ± 2.7	505 ± 3.4	380	460	530

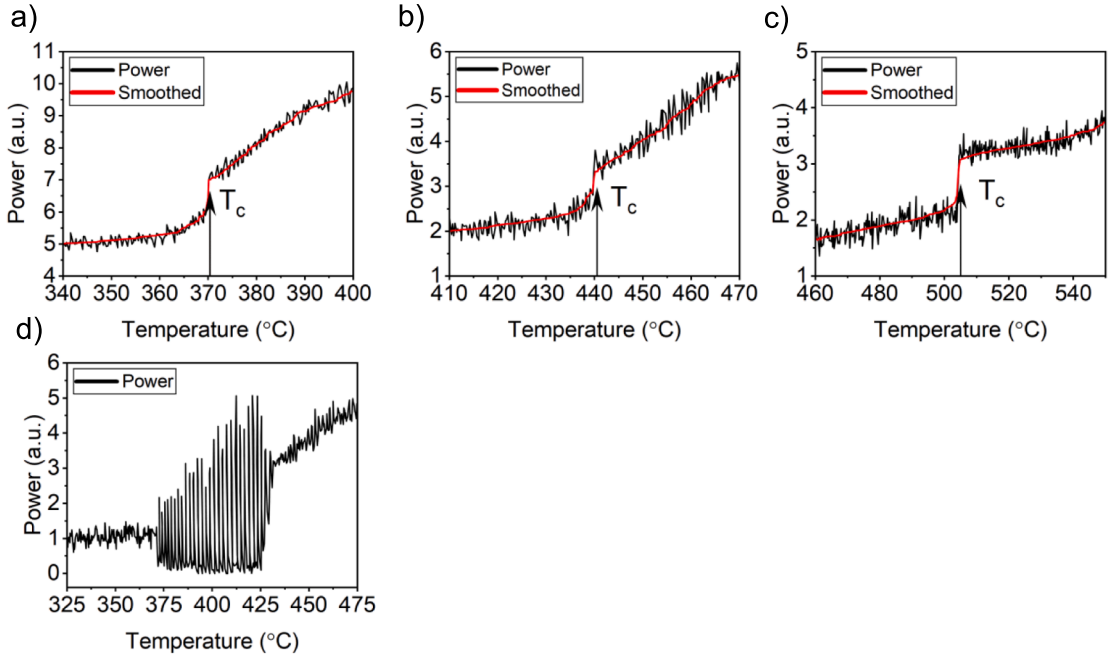

Fig. 10. Curie temperatures of alloys 42, 46 and 52 in (a), (b) and (c), respectively, and the transition region between alloy 42 and 46 in (d), of the graded wall.

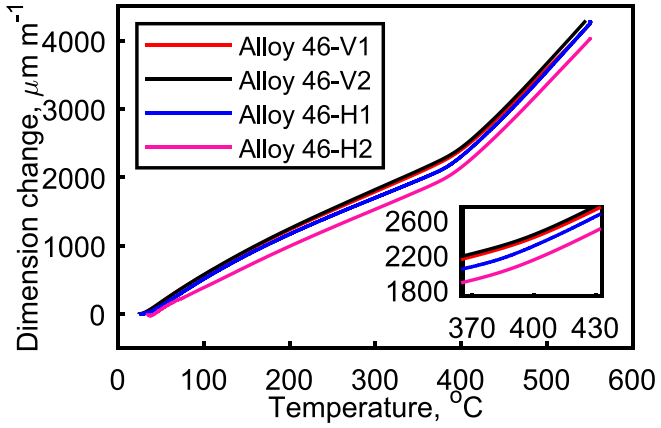

Fig. 11. Temperature-displacement curves of the as-deposited alloy 46 specimens oriented in the building (BD) and the welding directions (WD). Specimens named V and H correspond to the orientations along the BD and WD, respectively.

Table 7
Mean CTEs of the as-deposited LTE alloy 46 and the corresponding ASTM standard specification of the CTEs for the LTE alloy 46. The CTE values are in the unit of: $\times 10^{-6}\ ^{\circ}C^{-1}$.

Mean CTE	As-deposited, BD	As-deposited, WD	Commercial alloy 46 [41]
30–300 °C	7.84 ± 0.06	7.33 ± 0.24	7.5
30–400 °C	7.70 ± 0.05	7.32 ± 0.15	7.5
30–500 °C	8.89 ± 0.11	8.75 ± 0.15	8.5

our previous results regarding the mean CTE values of Invar 36 alloy deposited using WAAM (cold wire pulsed GTAW process) [21]. The direction related differences in the mean CTE values are most likely to occur due to the build-up of non-uniform residual stresses during WAAM. Wang et al. [37] showed that residual stress anisotropy can lead to an effective thermal expansion anisotropy. In addition, stress influences the magnetostriction of a magnetic material [38]. As the peculiarity in the thermal expansion behaviour of Fe-Ni alloys is due to the temperature-dependent compensation of the lattice thermal expansion by the spontaneous magnetostriction. Consequently, the thermal expansion of the Fe-Ni LTE alloys will be affected under the influence of stresses. The fabrication of products by WAAM is subject to the development of residual stresses due to the intrinsic thermal cycles imposed on the part during processing [39]. Yakout et al. [40] showed the presence of tensile residual stresses (upto 350 MPa) in Invar 36 parts manufactured by laser-powder bed fusion. The residual stress states of the deposits were not quantified in this study however, it is reasonable to assume the presence of residual stresses in the as-deposited alloy 46. Consequently, the anisotropy in the mean CTE values between the BD and WD oriented samples may be attributed to the influence of the stress state in the block on the thermal expansion of alloy 46. To comprehensively establish the correlation between residual stresses induced during the AM of Fe-Ni LTE alloys and their impact on thermal expansion, a dedicated study is recommended for future investigation. Additionally, it is worth noting that the directional thermal expansion anisotropy observed in the CTE measurements is low, possibly due to the redistribution of internal stresses during the machining of the dilatometry samples. However, in a practical application of an as-deposited LTE alloy structure, this effect could become more pronounced. Therefore, a stress-relieving heat treatment may be sufficient to mitigate the impact of stress on the thermal expansion of the as-deposited LTE alloys. Overall, the CTE values of the as-deposited alloy 46 are comparable to those of the conventionally processed alloy. The compositional stability is also reflected in the similar character of the temperature-displacement curves for the different samples. Lastly, Curie temperature measurements and chemical analysis are sufficient to validate the in-situ fabricated alloys as LTE alloys with the expected LTE behaviour. However, a separate block of alloy 46 was deposited in this study for a thorough investigation of the mean CTE values to determine whether a process like T-WAAM can affect the thermal expansion of the in-situ generated LTE alloys, potentially leading to unexpected results. Notably, the mean CTE values of alloy 46 were confirmatory with its commercial counterpart, implying that the mean CTE values of alloys 42 and 52 deposited in this work will be in line with what is expected from such LTE alloys. This extends to other LTE alloys that can be fabricated with the T-WAAM process, apart from the alloys deposited in this study. Accordingly, T-WAAM is a suitable processing method to generate on demand LTE alloys from the Fe-Ni system.

In summary, the continuous and intermittent metal transfer modes were identified during the T-WAAM process and are schematically illustrated in Fig. 12(a) and (b). The continuous metal transfer mode was characterised by the formation of a persistent liquid metal bridge that allows for the smooth transfer of Ni to the weld pool, resulting in a stable weld bead, as shown in Fig. 12(a). In contrast, the intermittent metal mode results in the formation of metal droplets at the tip of the Ni wire. The entry of these droplets into the weld pool can lead to instabilities, causing the weld bead to abruptly change spatially, as shown in Fig. 12 (b). Additionally, the flow in the weld pool is adequate to create a homogeneous distribution of Ni (Fig. 12(a)) in the weld bead deposited using the continuous transfer mode, as the Ni wire remains in contact with the weld pool throughout the deposition. Whereas, the time between two subsequent droplet detachment events during the intermittent metal transfer mode may lead to locally enriched regions (Fig. 12 (b)) of Ni in the weld bead, causing larger deviations from the desired Ni concentrations. Therefore, the continuous transfer mode was utilised to fabricate LTE Fe-Ni alloys using the T-WAAM process. Due to the stable deposition and optimum chemical mixing in this mode, the in-situ fabricated LTE Fe-Ni alloys exhibit thermal properties comparable to those of commercially available alloys. Consequently, the T-WAAM process can potentially be used to offset the challenges associated with the conventional processing of LTE Fe-Ni alloys, providing alloys with on-demand thermal expansion properties.

4. Conclusions

In this study, a twin-wire approach was used in the cold wire GTAW process to deposit multiple low thermal expansion alloy compositions. The key aspects pertaining to the deposition of the in-situ synthesised compositions such as, process stability, compositional control and the thermal properties were presented and discussed. The outcomes of this study lead to the following conclusions:

1. The T-WAAM process enables the customised synthesis of Fe-Ni alloy compositions with low thermal expansion, providing the flexibility to tailor the thermal expansion properties of structures and obtain commercially unavailable alloy compositions.
2. The microstructure of the as-deposited low thermal expansion alloys 42, 46, and 52 is characterised by columnar grains and the formation of a single-phase austenitic structure.
3. The continuous metal transfer mode exhibits enhanced process stability relative to the intermittent metal transfer mode during the T-WAAM process, owing to the lack of weld pool instabilities in this mode.
4. Good control over desired compositions is achievable, regardless of the dynamic nature of the T-WAAM process. This is attributed to the observed stability within the continuous metal transfer mode and the solid solution compatibility inherent in the Fe-Ni alloy system.
5. The low thermal expansion alloys fabricated in-situ through the T-WAAM process exhibit Curie temperatures and mean coefficients of thermal expansion that are comparable with those observed in conventionally produced alloys.

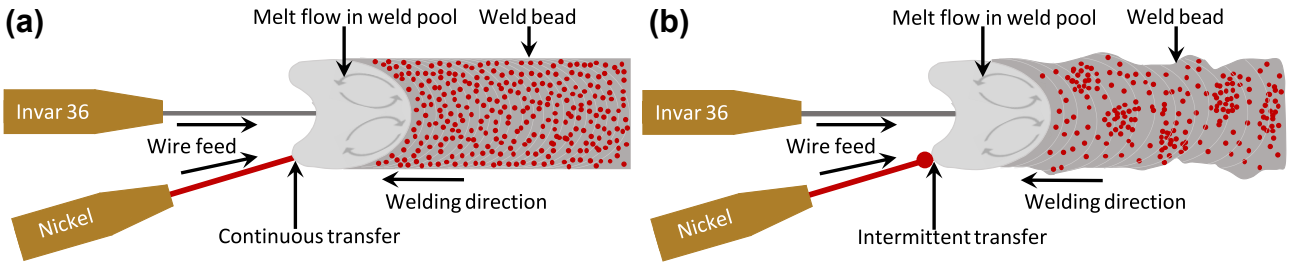

Fig. 12. Schematic description of the continuous metal transfer mode in (a) and intermittent metal transfer mode in (b), and the effects of these respective modes on the deposition and chemical stability during the T-WAAM process.

Although demonstrated here for Fe–Ni alloys, the combined method of T-WAAM and in-situ alloying is in principle applicable to fabricate other multi-element alloys by compositional design, which will allow to expand the application fields of WAAM.

CRediT authorship contribution statement

Arjun Sood: Writing – original draft, Visualization, Validation, Resources, Methodology, Investigation. **Jim Schimmel:** Resources, Methodology, Investigation. **Marko Bosman:** Resources, Funding acquisition. **Constantinos Goulas:** Writing – review & editing, Supervision, Resources, Funding acquisition. **Vera Popovich:** Writing – review & editing, Supervision, Resources. **Marcel J.M. Hermans:** Resources, Writing – review & editing, Supervision, Project administration.

Declaration of competing interest

The authors declare that they have no known competing financial interests or personal relationships that could have appeared to influence the work reported in this paper.

Data availability

Data will be made available on request.

Acknowledgements

This work was supported by the European Union's Horizon 2020 research and innovation programme under grant agreement no. 862017. This research is also supported by the Materials innovation institute M2i (www.m2i.nl). This publication reflects only the author's view and the commission is not responsible for any use that may be made of the information it contains. Ruud Hendrikx at the Department of Materials Science and Engineering of the Delft University of Technology is acknowledged for the XRD analysis.

References

[1] A. Sahoo, V.R.R. Medicherla, Fe-Ni invar alloys: a review, in: Materials Today: Proceedings, Elsevier Ltd, 2020, pp. 2242–2244, https://doi.org/10.1016/j.matpr.2020.12.527.
[2] E. F. Wassermann, The Invar problem, 1991.
[3] M. Yakout, A. Cadamuro, M.A. Elbestawi, S.C. Veldhuis, The selection of process parameters in additive manufacturing for aerospace alloys, Int. J. Adv. Manuf. Technol. 92 (5–8) (Sep. 2017) 2081–2098, https://doi.org/10.1007/s00170-017-0280-7.
[4] K. Wei, et al., Mechanical properties of invar 36 alloy additively manufactured by selective laser melting, Mater. Sci. Eng. A 772 (Jan. 2020), https://doi.org/10.1016/j.msea.2019.138799.
[5] Low-expansion alloys introduction and overview. [Online]. Available: http://ebookcentral.proquest.com/lib/delft/detail.action?docID=3002339.
[6] S. Chikazumi, T. Mizoguchi, N. Yamaguchi, P. Beckwith, The invar problem, J. Appl. Phys. 39 (2) (1968) 939–944, https://doi.org/10.1063/1.1656337.
[7] D.A. Colling, W.J. Carr, Invar anomaly, J. Appl. Phys. 41 (13) (1970) 5125–5129, https://doi.org/10.1063/1.1658625.
[8] "Low-Expansion alloys," *ASM Handbook Volume 2:Properties and Selection: Nonferrous Alloys and Special-Purpose Materials*, vol. 2. ASM International, p. 889, 1990. doi: 10.1361/asmhba0001099.
[9] M. Shiga, 340 Invar alloys.
[10] H. Asgari, M. Salarian, H. Ma, A. Olubamiji, M. Vlasea, On thermal expansion behavior of invar alloy fabricated by modulated laser powder bed fusion, Mater. Des. 160 (Dec. 2018) 895–905, https://doi.org/10.1016/j.matdes.2018.10.025.
[11] B. Mills, Machinability of engineering materials, Springer Science & Business Media, Dordrecht, 2012.
[12] K. Treutler and V. Wesling, "The current state of research of wire arc additive manufacturing (Waam): A review," *Applied Sciences (Switzerland)*, vol. 11, no. 18. MDPI, Sep. 01, 2021. doi: 10.3390/app11188619.
[13] B. Tomar, S. Shiva, T. Nath, A review on wire arc additive manufacturing: Processing parameters, defects, quality improvement and recent advances, Materials Today Communications, vol. 31. Elsevier Ltd, Jun. 01, 2022. doi: 10.1016/j.mtcomm.2022.103739.
[14] C. Zhang, et al., Additive manufacturing of functionally graded materials: a review, Mater. Sci. Eng. A 764 (Sep. 2019), https://doi.org/10.1016/j.msea.2019.138209.
[15] R. Singh, V. Bhavar, P. Kattire, S. Thakare, S. Patil, R.K.P. Singh, A review on functionally gradient materials (FGMs) and their applications", in IOP conference series: materials science and engineering, Institute of Physics Publishing (2017), https://doi.org/10.1088/1757-899X/229/1/012021.
[16] Y. Ayan, N. Kahraman, Fabrication and characterization of functionally graded material (FGM) structure containing two dissimilar steels (ER70S-6 and 308LSi) by wire arc additive manufacturing (WAAM), Mater. Today Commun. 33 (Dec. 2022), https://doi.org/10.1016/j.mtcomm.2022.104457.
[17] L.D. Bobbio, et al., Additive manufacturing of a functionally graded material from Ti-6Al-4V to invar: experimental characterization and thermodynamic calculations, Acta Mater. 127 (Apr. 2017) 133–142, https://doi.org/10.1016/j.actamat.2016.12.070.
[18] L.D. Bobbio, et al., Experimental analysis and thermodynamic calculations of an additively manufactured functionally graded material of v to invar 36, J. Mater. Res. 33 (11) (Jun. 2018) 1642–1649, https://doi.org/10.1557/jmr.2018.92.
[19] D.C. Hofmann, et al., Developing gradient metal alloys through radial deposition additive manufacturing, Sci. Rep. 4 (Jun. 2014), https://doi.org/10.1038/srep05357.
[20] T.A. Rodrigues, et al., Steel-copper functionally graded material produced by twin-wire and arc additive manufacturing (T-WAAM), Mater. Des. 213 (Jan. 2022), https://doi.org/10.1016/j.matdes.2021.110270.
[21] A. Sood, et al., Directed energy deposition of invar 36 alloy using cold wire pulsed gas tungsten arc welding: effect of heat input on the microstructure and functional behaviour, J. Mater. Res. Technol. 25 (Jul. 2023) 6183–6197, https://doi.org/10.1016/j.jmrt.2023.06.280.
[22] Arcelor Mittal, M93 PIPES AND TUBES FOR LNG TRANSFER LINES-WELDING PROCESSES (Stainless & Nickel Alloys). Accessed: Jul. 21, 2023. [Online]. Available: https://www.spacematdb.com/spacemat/manudatasheets/Invar%20M93.pdf.
[23] ASTM International, Standard Test Method for Linear Thermal Expansion of Solid Materials by Thermomechanical Analysis 1, 2019, doi: 10.1520/E0831-19.
[24] Y. Yehorov, L.J. da Silva, A. Scotti, Balancing WAAM production costs and wall surface quality through parameter selection: a case study of an Al-Mg5 alloy multilayer-non-oscillated single pass wall, J. Manuf. and Mater. Proces. 3 (2) (Jun. 2019), https://doi.org/10.3390/jmmp3020032.
[25] T. DebRoy et al., Additive manufacturing of metallic components – Process, structure and properties, Progress in Materials Science, vol. 92. Elsevier Ltd, pp. 112–224, Mar. 01, 2018. doi: 10.1016/j.pmatsci.2017.10.001.
[26] S. Kou, Welding metallurgy second edition, 2003. [Online]. Available: www.copyright.com.
[27] H. Tan, et al., Investigation on microstructure and properties of laser solid formed low expansion invar 36 alloy, J. Mater. Res. Technol. 9 (3) (2020) 5827–5839, https://doi.org/10.1016/j.jmrt.2020.03.108.
[28] F. Veiga, A. Suárez, T. Artaza, E. Aldalur, Effect of the heat input on wire-arc additive manufacturing of invar 36 alloy: microstructure and mechanical properties, Welding in the World 66 (6) (Jun. 2022) 1081–1091, https://doi.org/10.1007/s40194-022-01295-4.
[29] H. Asgari, M. Salarian, H. Ma, A. Olubamiji, M. Vlasea, On thermal expansion behavior of invar alloy fabricated by modulated laser powder bed fusion, Mater. Des. 160 (Jul. 2018) 895–905, https://doi.org/10.1016/j.matdes.2018.10.025.

[30] C. Qiu, N.J.E. Adkins, M.M. Attallah, Selective laser melting of invar 36: microstructure and properties, Acta Mater. 103 (Jan. 2016) 382–395, https://doi.org/10.1016/j.actamat.2015.10.020.
[31] W.C. Leslie, E. Hornbogen, Chapter 17 – Physical metallurgy of steels, in: Physical Metallurgy, Fourth Edition, R. W. Cahn, P. Haasen (Eds.), Oxford: North-Holland, 1996, pp. 1555–1620. doi: https://doi.org/10.1016/B978-044489875-3/50022-3.
[32] A. Verma, M. Sundararaman, J.B. Singh, S.A. Nalawade, A new method for determining the curie temperature using a dilatometer, Meas. Sci. Technol. 21 (10) (2010) pp, https://doi.org/10.1088/0957-0233/21/10/105106.
[33] L.L. Harner, Controlled expansion alloys. Accessed: Sep. 04, 2023. [Online]. Available: https://www.carpentertechnology.com/blog/selecting-controlled-expansion-alloys.
[34] M. Tsuda, Effect of minor alloying elements on the mean thermal expansion coefficient of Fe-36% Ni invar alloy, Tetsu-to-Hagane 80 (12) (1994) 944–949, https://doi.org/10.2355/tetsutohagane1955.80.12_944.
[35] V. M. Kalinin, F. N. Dunaev, and V. A. Kornyakov, "Effect of alloying elements point of Fe-Ni invar alloys, 1970.
[36] C. Chen, B. Ma, S. Miao, B. Liu, Effect of cobalt on microstructure and mechanical properties of invar alloy, in lecture notes in mechanical engineering, Pleiades J. (2018) 855–864, https://doi.org/10.1007/978-981-13-0107-0_84.
[37] X.L. Wang, C.M. Hoffmann, C.H. Hsueh, G. Sarma, C.R. Hubbard, J.R. Keiser, Influence of residual stress on thermal expansion behavior, Appl. Phys. Lett. 75 (21) (Nov. 1999) 3294–3296, https://doi.org/10.1063/1.125329.
[38] B. D. Cullity and C. D. Graham, "Introduction to magnetic materials second edition introduction to magnetic materials.
[39] Q. Wu, T. Mukherjee, A. De, T. DebRoy, Residual stresses in wire-arc additive manufacturing – hierarchy of influential variables, Addit. Manuf. 35 (Oct. 2020), https://doi.org/10.1016/j.addma.2020.101355.
[40] M. Yakout, M.A. Elbestawi, "Residual stress formation in laser-based powder bed fusion (PBF-LB) of invar 36", in ASTM special technical publication, ASTM International (2020) 34–44, https://doi.org/10.1520/STP163120190149.
[41] ASTM International, Standard specification for iron-nickel sealing alloys, 2017, doi: 10.1520/F0030-96R17.